An edited version of this paper was published by AGU.

Evidence of strong inertia-gravity wave activity during the POMME experiment

Pascale Bouruet-Aubertot[1], H. Mercier[2], F. Gaillard[2], and P. Lherminier[2]

1 : Laboratoire d'Océanographie et du Climat: Expérimentations et Approches Numériques/Institut Pierre-Simon Laplace, UMR 7617, Centre National de la Recherche Scientifique/Université Pierre et Marie Curie/Institut de Recherche pour le Développement, Paris, France

2 : Laboratoire de Physique des Océans, UMR 6523, Centre National de la Recherche Scientifique/Institut Français de Recherche pour l'Exploitation de la Mer/Université de Bretagne Occidentale, Plouzané, France

Abstract:

The purpose of this paper is to characterize inertia-gravity waves (IGW) activity and to investigate the variability of these waves in relationship to atmospheric forcing and larger-scale motions. To this aim, we analyzed Eulerian measurements of horizontal currents and temperature collected over 1 year during the Programme Océan Multidisciplinaire Méso Echelle (POMME). We focused on the main frequency components of the IGW spectrum, namely the inertial frequency f and the semidiurnal frequency M2. Time evolution of the relative energy of these two components gave evidence of isolated events of high intensity. We performed a detailed analysis of these events and identified mechanisms of generation of these waves. Localized spots of intense, near-inertial IGW were observed in winter. During the mixed layer deepening, one event was correlated with plume-like structures resulting from peaks of intense surface cooling. This suggests a local generation process driven by strong downward vertical motions. Instead, other events of strong IGW could be related to submesoscale features, characteristic of a frontal region, in particular, wave trapping within anticyclonic eddies. In contrast, a downward energy propagation down to about 500 m below the mixed layer was isolated after a stormy period. Eventually, internal tidal beams, possibly generated at a nearby seamount, intermittently crossed the mooring, though less energetically than the previous events. Last, we estimated the eddy diffusivity from the velocity vertical shear. Large variations were obtained, from 10^{-6} m2/s up to 10^{-3} m2/s, consistent with the intense events previously isolated.

Abstract

The purpose of this paper is to characterize inertia-gravity waves (hereafter IGW) activity and to investigate the variability of these waves in relationship with atmospheric forcing and larger scale motions. To this aim we analyzed Eulerian measurements of horizontal currents and temperature collected over one year during POMME experiment. We focused on the main frequency components of the IGW spectrum, namely the inertial frequency f and the semi-diurnal frequency $M2$. Time evolution of the relative energy of these two components gave evidence of isolated events of high intensity. We performed a detailed analysis of these events and identified mechanisms of generation of these waves. Localized spots of intense, near-inertial, IGW were observed in winter. During the mixed layer deepening one event was correlated with plume-like structures resulting from peaks of intense surface cooling. This suggests a local generation process driven by strong downward vertical motions. Instead, other events of strong IGW could be related to submesoscale features, characteristic of a frontal region, in particular wave trapping within anticyclonic eddies. In contrast a downward energy propagation down to about $500m$ below the mixed layer was isolated after a stormy period. Eventually internal tidal beams, possibly generated at a nearby sea-mount, intermittently crossed the mooring, though less energetic than the previous events. Last we estimated the eddy diffusivity from the velocity vertical shear. Large variations were obtained, from $10^{-6}m^2/s$ up to $10^{-3}m^2/s$, consistently with the intense events previously isolated.

1. Introduction

Understanding and quantifying the processes that drive TS variability in the upper layers was one of the main objectives of the POMME experiment. This question is of particular importance in an area where formation and subduction of the Subpolar Mode Water occur (Paillet

and Mercier, 1997). The atmospheric forcing, both thermodynamic and mechanical, obviously plays a major role in the subduction process (Woods and Barkmann, 1986). Nevertheless the background meso-scale field contributes to this process. Indeed these motions are responsible for part of the mixed layer variability that is related to subduction. In the North Atlantic this impact of meso-scale motions was quantified using a GCM by Valdivieso Da Costa *et al.* (2005). Emphasis on these mesocale processes influencing subduction and primary production was thus given in the experiment (Reverdin *et al.*, 2004, Giordani *et al.*, 2004.b). Nevertheless motions at smaller scales, namely submesoscale, are to be considered. In particular, regions of large vertical velocities resulting from filamentation of meso-scale structures, could increase subduction rates significantly (Paci *et al*, 2004). Quite naturally this leads to consider as well inertia-gravity waves (hereafter referred to as IGW). In the upper ocean generation of these waves mainly results from an indirect excitation by the wind (D'Asaro, 1985) through horizontally convergent motions in the mixed layer (e.g. D'Asaro et al, 1995.b). This energy input from the atmospheric forcing into inertia-gravity waves can provide a dynamical pathway that eventually contributes to surface and deeper layers exchanges. These exchanges are mainly driven by vertical turbulent mixing that contributes to subduction processes. Also the presence of a meso-scale eddy field can influence the propagation of these waves (e.g. Klein and Llewellyn Smith, 2001), leading to wave focusing and trapping (Kunze and Sanford, 1984, Kunze et al, 1995). Eventually, another pathway for IGW is through spontaneous generation during geostrophic adjustment (e.g. Tang, 1979) thus possibly involving the mesoscale eddy field. The full picture is then a complex one involving the atmospheric forcing as a main energy source for IGW evolving within a background mesoscale field that could both strongly influence the propagation of these waves and generate them.

In this context our purpose is to characterize the IGW field in order to estimate the impact of these waves in terms of energy fluxes into the interior and vertical mixing. This analysis will benefit from the knowledge of the atmospheric forcing and information on the mesoscale eddy field as inferred from Lagrangian float trajectories and inverse models implemented during POMME. Our analysis is based on Eulerian data collected over 13 months at the northern boundary of the domain (Fig.1), consisting of ADCP (Acoustic Doppler Current Profiler) and temperature data in the upper $500m$ with a few current and temperature data down to $4000m$.

This paper is organized as follows: we describe in section 2 the mooring chain we focus on, at the northern boundary of the POMME domain, and give some details on the data sampling and post-processing. An overview of the temporal evolution of the atmospheric forcing and mesoscale oceanic motions, which both constitute potential sources for IGW, is then introduced in section 3. The evolution of supra-inertial kinetic energy content is described as well. We then infer the occurrence of IGW of high amplitude from the time evolution of the two prevailing frequencies, the inertial frequency, f and the semi-diurnal frequency, $M2$. A detailed analysis of these events is conducted in section 4 with a focus on winter-time events. The impact of the events on vertical turbulent mixing is then addressed in section 5. To do so the vertical eddy diffusivity is inferred from the velocity vertical shear. Discussion and conclusion are the subject of section 6.

2. Measurements at the North mooring

We analyze the 13 month data (from Sept. 22th, 2000 until Oct. 22th, 2001) collected at the North mooring, $45N - 18W$, located at the middle of the northern boundary of the POMME region, about 1.5^o to the North of the Azores-Biscay Ridge summit (Fig.1). The bathymetry is typical of a ridge spur with several seamounts identified in the vicinity of the mooring site

that was located in a valley with bottom depth equals to $4840m$. In the upper $500m$ current time series with a $16m$ vertical resolution are available from a $75\ kHz$ RD Instruments ADCP. However we focused our analysis in the depth range $[240, 480]\ m$ where the time sampling of the measurements was regular enough for a statistical analysis. In addition, six temperature time series within $[185, 435]\ m$ were obtained with a vertical separation of $50m$ from Wadar T sensors and, at the upper most level, from a Seacat from Seabird Instruments that also provided salinity data. For the rest of the water column four RCM8 AAnderaa current and temperature meters were at 752, 1052, 2552 and 4051 meter depth. The temporal sampling after data processing is equal to $1h$ for the ADCP data, to $30min$ for the AAnderaa current and temperature meters and to $15min$ for the Wadar and Seacat time series.

3. Overview of the temporal evolution

In this section we give an overview of the time evolution of the atmospheric forcing and of the meso-scale circulation as inferred from sub-diurnal motions, which both constitute a source for IGW either by indirect excitation for the atmospheric forcing or through geostrophic adjustment for the eddies.

3.1. Large-scale context and background stratification

Wind stress and surface heat fluxes were computed using a synthetic approach by Caniaux *et al* (2004). These quantities are represented in Figure 2 over the time interval ranging from Sept. 22th, 2000 to Oct. 22th, 2001. As expected the net surface heat flux decreases in Autumn with low negative values until the beginning of January (about day 100). Meanwhile and until the end of February (day 150) episodes of strong winds are encountered. The strong variations in the wind stress associated with these events are likely to lead to IGW generation. Then, from

mid-January until the end of June, the net heat flux gradually increases before decreasing again. The net heat flux changes sign on March 6th, 2001 (day 165). At that time, the mixed layer depth is at a maximum and the subsequent warming results in a rapid decrease in the mixed layer depth (Fig.2.d). Over all these spring and summer months winds are much weaker though a few periods of stronger winds are noticed- but of less intensity than in winter.

The time evolution of the stratification is documented, with six temperature time series in the upper layer and a salinity time series at the upper level, $z = 185m$, as well as with (T, S) profiles, at different locations in the POMME area, taken during four cruises (P0, Sept.2000; P1, Feb.2001; P2, April 2001; P3, Sept.2001). Thus, we get some insights on the variability of the stratification from the vertical temperature gradient, $\partial_z T$ (Fig.3). Until the beginning of November ($t \sim 50d$) the vertical temperature gradient is fairly weak while during the second half of the autumn ($t \sim 50 - 100d$) bursts of stronger stratification are observed, which sometimes extend down to $400m$ (e.g. at $t \sim 70 - 75d$ in Fig.3). This evolution occurs during the deepening of the mixed layer during a period of minimum net heat flux (Fig.2.a). Indeed the mixed layer depth typically varies from $\sim 30m$ down to $\sim 150m$ from September to December in the Northern area of POMME (Fig.2.d). Note that because of the short duration -less than a day- of these more stratified bursts it is unlikely that they could be the signature of a passing-by eddy. Next, from mid-January and over the next two months, ($t \sim 110 - 180d$), a strong variability is observed, in the upper $300m$, that takes the form of water patches of almost homogeneous temperature. These plume-like structures, lasting for a few days, suggest mixed layer intrusions that can be seen in Figure 2.d (see section 4.2 as well). Meanwhile, below, at depths $z \sim 350m$, spots of strong vertical temperature gradients are observed. Then, while the mixed layer shallows,

the variability of the temperature gradient remains weak until the end of August ($t \sim 345d$). Finally a period of strong vertical temperature gradient is observed from mid-September until mid-October.

An overview of sub-diurnal motions, based on a 2-day averaging of the ADCP data, is given by a vector plot as a function of time and depth (Fig. 4). This plot provides insights on the eddy activity since the annual mean current is small as in the climatology, of less than $4cm/s$, and directed towards the South-East in the upper layer (Paillet and Mercier, 1997). Superimposed to this mean circulation, a variability at higher frequency is noticed during autumn and winter that can be attributed to eddy motions. Then weaker currents are later observed until the next autumn. More precisely the time evolution of the vertically averaged horizontal kinetic energy (Fig. 5.a) shows two maxima of about $300cm/s^2$ around day 50 (mid-November) and later within $[160 - 180]$ (beginning of March). Eventually an increase in kinetic energy is observed at the beginning of the following autumn (Fig.5). Note the peaks in sub-diurnal kinetic energy during stormy periods when IGW are likely to be generated. As a consequence interactions between IGW and energetic mesoscale motions as well as spontaneous generation are likely to take place during these time intervals.

3.2. Supra-inertial oceanic motions

Time evolution of the vertically averaged horizontal kinetic energy of supra-inertial motions shows a strong variability (Fig.5.b). In particular four bursts of high horizontal kinetic energy occur during autumn and winter: around mid-October (days $15 - 25$), and from February until mid-March (days 130, 140 and $170 - 180$). These peaks can be either related to storms and/or to a high level of sub-diurnal kinetic energy. Indeed, in February-March, some of the events are

simultaneously observed with a high level of sub-diurnal horizontal kinetic energy.

We next computed frequency spectra of kinetic energy. As expected two main peaks, around the inertial and semi-diurnal frequencies, were obtained (e.g. van Haren, 2004). Thus, we focused on the time evolution of the energy content in the two frequency bands $[0.9f, 1.1f]$ and $[0.9M2, 1.1M2]$ as a simple means to detect events of strong IGW. To this aim we performed wavelet transforms of the current time series that is able to track short time duration intense events. Figure 6 represents the time-depth evolution of the amplitudes of the velocity in these two frequency bands. For clarity, we plot separately the ADCP data (Fig.6.a and c), with a regular vertical separation of $16m$, and the AAnderaa current meter data which are sparse, the depths of the measurements being indicated by the arrows (Fig.6.b and d). Note that the deepest current meter data, $z = 4051m$, are not taken into account in this figure because of their very small signature. In the upper layer three main events of strong near-inertial waves are clearly identified in Figure 6.a at the beginning of October ($day \sim 20$) and during winter ($days \sim 130 - 140$ and $days \sim 170 - 180$). Unsurprisingly we retrieve the events inferred from the supra-inertial averaged kinetic energy (Fig.5.b). However the focus on the f component shows that the events differ regarding their depth distribution: while an almost continuous distribution is observed during the first stormy period, localized spots are observed during winter. Deeper, at depths $752m$ and $1052m$, spots of high f amplitude are observed during the same periods as the upper depth events already mentioned (Fig.6.b). However a close correlation with the upper depth events is not expected since the generation zones differ. In contrast the $M2$ signal is weaker, with a maximum amplitude about half that of the f component but more $M2$ events are observed (Fig.6.c). $M2$ events are observed over most of the year but with more intensity during

autumn ($days \sim 60 - 100$ and $350 - 390$) and winter ($days \sim 160 - 200$). Deeper, at depths $752m$ and $1052m$, localized spots are observed as well mostly in autumn and winter (Fig.6.d)

4. Focus on events of high amplitude inertia-gravity waves

We present in this section a detailed analysis of three episodes of high amplitude waves presumably of different origin. The first episode occurs at the beginning of fall and is related to storms. During the second episode that takes place during winter near-inertial waves are either induced by overlying convective plumes or trapped within anticyclonic eddies. The third episode gives evidence of internal tides.

4.1. Storm generated near-inertial waves

The horizontal components of the velocity filtered in the near-inertial frequency band $[0.9f, 1.1f]$ during the first strong episode of near-inertial waves are displayed in Figure 7. Evidence of two events at days 15 and 22 respectively, first occurring at depth $z = 240m$, is seen in Figure 7. The phase tilting upward indicates a downward energy propagation (Fig.7).

In order to estimate quantitatively the downward energy propagation of these events we computed the correlation coefficient of the complex near-inertial velocity, D, within the time interval $[10 - 40]$ days, with a reference depth at the upper level $z_1 = 240m$. This coefficient is computed using the following expression, (see as well Qi $et\ al$ (1995), their Eq.(8)):

$$\Gamma_{z_1-z_2}(\tau) = \frac{< D_{z_1}^*(t) D_{z_2}(t + \tau) >}{\sqrt{< D_{z_1}^*(t) D_{z_1}(t) >} \sqrt{< D_{z_2}^*(t + \tau) D_{z_2}(t + \tau) >}} \qquad (1)$$

The modulus of this complex correlation coefficient is displayed as a function of the delay τ and depth in Figure 8. The maximum correlation value follows a straight line consistently with a downward energy propagation. Thus, we estimated the vertical group velocity from the slope

of this line. A value of $1mm/s = 86.4m/d$ is obtained. The mean horizontal kinetic energy of the f component during this time interval, $15d - 22d$, is equal to $4\,J/m^3$, to be compared with a $14\,J/m^3$ mean value for the total horizontal kinetic energy and with a $9\,J/m^3$ mean value for sub-diurnal kinetic energy. The vertical flux of horizontal kinetic energy for the f component is thus of the order of $4mW/m^2$. Note that due to a lack of resolution of near surface currents we could not compare this value with the energy flux associated with mixed layer motions. These results suggest that these waves were generated from the base of the mixed layer after a storm.

To check the relevance of this hypothesis we estimated the time required for the waves to propagate from the base of the mixed layer down to the observed data. To this aim, we assumed a WKB scaling that provides an estimate of the variation along the vertical of the vertical group velocity, however strictly valid if the typical vertical wavelength is smaller than the scale of variation of the medium. In this framework the vertical group velocity varies inversely with the buoyancy frequency (e.g. Qi *et al*, 1995, Leaman and Sanford, 1975): $cg_z(z) = cg_\zeta \frac{N_r}{N(z)}$, where cg_ζ is a constant, computed from the value of $cg_z = 1mm/s$ at depth $z = 400m$, N_r is a reference buoyancy frequency -equal to $5.10^{-3}rad/s$- and $N(z)$ the buoyancy frequency profile estimated from ship stations in this area in September. A value of about 5 days was obtained for the signal to propagate from $z = 20m$ down to $z = 240m$. This is quite consistent with the wind stress time evolution (Fig.2.a) which shows 2 peaks at days 11 and 18 that can have led to the wave groups observed at days 15 and 22 at $z = 240m$. Note however the uncertainty of the estimate which relies on WKB scaling, and neglects the meso-scale eddy field and currents which influence inertia-gravity wave propagation.

4.2. Energetic events during winter

We focus on the energetic waves that were observed between January and the end of March. Evidence of these waves is given in Figure 9.a by a succession of spots of high amplitude of the f component, around days 130, 140, 170 and 185. These events last typically less than 3 days and are localized along the vertical except for the day-170 event. The lack of vertical coherence, contrary to what is observed for instance when storm generated IGW, suggests that these waves are of different origin. Indeed these intense wave events might be related either to the strong variability of the stratification or to the mesoscale eddy field as shown by the high level of sub-inertial kinetic energy. More precisely, until about the end of February (day 150), well-mixed patches at upper depth (Fig.3), possibly associated with mixed layer intrusions, suggest that the strong variability of the deep winter mixed layer might play a role in IGW generation. Alternatively these intense events might be identified as near-inertial waves trapped within anticyclonic eddy structures (e.g. Kunze and Sanford, 1984). The frequency of these waves is slightly subinertial because of the background anticyclonic vorticity which explains why trapping can result. To address this point we applied the method described by Lilly and Rhines (2002) in order to isolate eddies, when the frequency of the waves is slightly sub-inertial. This second mechanism could be of relevance in particular for the events that occur after mixed layer shallowing.

In order to get further insights into the mixed layer variability, and especially into the plume-like structure (fig.3), the net and latent heat fluxes (Caniaux et al, 2004.a and b) were analyzed. As shown in Figure 10.a there is a net heat loss for the ocean until approximately day 160. During this period -beginning of January until beginning of March- winter surface cooling, mainly driven by evaporation, leads to a deepening of the mixed layer. Interestingly peaks of minimum

net heat flux are observed simultaneously to the low stratification events for time around days $120 - 130$, 135, which could confirm the hypothesis of plume-like structures. Furthermore the intrusion of the mixed layer down to the measurement depth interval was revealed by subsurface measurements by a Carioca buoy. Indeed the correspondence between the sub-surface temperature around days $151 - 153$ and the $z = 185m$ temperature, with a temperature difference less than 0.1^oC, shows that the mixed layer extends at least down to $185m$ (Fig.10.b). Note that these observations are consistent with the mixed layer depth variation during this period as inferred from an inverse model (Fig.2.d, see Gaillard *et al*, this issue). Indeed in this simulation the mixed layer deepens until the beginning of March ($day \sim 150$), reaching a maximum value of about $300m$ in this area.

To address the question of the relationship between plume-like structure and strong IGW more precisely we represented the vertical velocity averaged over two inertial periods in Figure 9.b[1]. This reveals that the regions of the most negative vertical velocities, around days $120 - 130$ and $150 - 155$ are associated with these plumes (Fig.3). In one case, around day 130, near-inertial waves are observed just below. Note that the frequency of these waves is slightly supra-inertial, $\sim 1.04f$, for this event which excludes a possible trapping within an anticyclonic eddy. Instead measurements suggest that the impinging convective plume leads to the generation of IGW in the underlying stratified fluid. We focused here on the amount of energy in the near-inertial frequency band but it is worthwhile to mention that an increase in the energy level at high frequency ($> 1.1M2$) is observed as well.

In contrast, this mechanism of generation is less convincing for the other event, around day 140, owing to a weaker downward vertical velocity within the plume. The slightly sub-inertial frequency of this event, $\sim 0.9f$, rather suggests wave trapping. In fact the hodograph of the veloc-

ity averaged over two inertial periods reveals strong changes in the velocity direction (Fig.11.a). Moreover these changes are consistent with an East- North East advection of a sub-mesoscale anticyclonic eddy through the mooring. A section in a vertical plane parallel to this horizontal advection direction, with isotherms superimposed, confirms that the azimuthal velocity is that of an anticyclonic eddy (Fig.11.b). The estimated radius of the eddy is of $6km$, that is of sub-mesoscale, with a vorticity of the order of $0.2f$. Hence, according to this rough estimate, the effective inertial frequency is reduced by about 10% which is consistent with the frequency of the observed waves. Similarly the event observed just before day 170 has a slightly subinertial frequency ($\sim 0.9f$) that can be correlated as well with the East- South East advection of an anticyclonic structure (Fig.11.c and d). The last event observed around day 180 is slightly supra-inertial. Nevertheless, these last two events have some similarity, both being related to the occurrence of 3 peaks in temperature with a temperature jump of 1^oC (Fig.10). Meanwhile an increase in salinity is observed at $z = 185m$. This variation is consistent with the T-S relationship in this region. The resulting density variation is a decrease of about $0.15\,kg/m^3$. In between the density reaches its maximum value close to 1027.1 which is as well the maximum surface density value as mentioned by Reverdin *et al* (2004). These strong density variations are typical of a frontal region. Indeed reanalyses performed by Assenbaum and Reverdin (2004) show that the mooring lies in a region between a northern cyclonic eddy and a southern anticyclonic region. These reanalyses are thus consistent with the eastward advection of sub-mesoscale eddies previously shown.

In summary, when the ADCP data lied within the 'boundary' between the mixed layer and the stratified water, we got evidence of plume-like structures, induced by surface cooling, that quite

likely acted as wave generators at the base of the mixed layer: the associated strong downward vertical motions leading to IGW generation just below. Later, after the shallowing of the mixed layer, observations indicate that strong IGW are related to submeso-scale structures, in particular near-inertial waves trapping within anticyclonic structures.

4.3. Evidence of intermittent internal tides

The second dominant frequency component is the semi-diurnal frequency, M2, of maximum amplitude about half that of the inertial frequency (Fig.6). We focus here on the time period between December $5th$ (day 75) and the end of December (day 95). The amplitude of the velocity in the frequency band $[0.9M2, 1.1M2]$ is displayed in Figure 12.a over this time interval as a function of time and depth. Localized events of high amplitude can be seen. Their vertical distribution, spots, suggests that internal tidal beams go through the mooring intermittently. The upward energy propagation within these beams is enlightened on filtered velocity plots (Fig.12.b) and is quantitatively evidenced by the anticyclonic rotation of velocity in the direction of phase propagation (increasing depths). These beams would be generated in a region of "adequately" varying topography and, depending on the stratification and currents, would propagate across the mooring. To check this possibility we performed a simplified ray tracing, taking into account the vertical variation of N only: $\Delta x/\Delta z = \sqrt{(N^2 - \omega^2)/(\omega^2 - f^2)}$ and then, from the ray path in a vertical plane, we searched for possible sites of generation. Among the different sea mounts in the area (Fig.1) one located at $(45.4N, 18W)$, namely $45km$ from the mooring, with a summit at $3700m$ depth is a possible candidate. Nevertheless the more detailed analysis of internal tide generation that would be required to confirm this scenario can not be conducted with the available data set collected during POMME.

5. Estimates of vertical eddy diffusivity and link with individual events and large scale forcing

The vertical eddy diffusivity, K, is classically related to kinetic energy dissipation rate, ϵ, following Osborn (1980): $K = \Gamma \epsilon / N^2$ where Γ is a mixing efficiency assumed to be constant. We use here this formulation but replacing the kinetic energy dissipation by a finescale parameterization based on vertical shear (e.g. Gregg, 1989). Our computation is based on the Polzin and Firing (1997) formulation, namely :

$$K = \Gamma \frac{\epsilon}{N^2} = \Gamma \frac{\epsilon_0}{N_0^2} \frac{f}{f_0} E^2 \tag{2}$$

with Γ, the mixing efficiency of a value of 0.2, $\epsilon_0 = 7.8 \, 10^{-10} \, W/kg$, a reference kinetic energy dissipation rate, $N_0 = 3 \, cph$, a reference buoyancy frequency, f_0, the inertial frequency at $30 \, dg$ latitude, and E is the shear spectral level normalized to the GM76 spectrum. Note that time-dependent buoyancy frequency values were inferred from an inverse model (Gaillard *et al.*, this issue) and the shear spectral level was estimated from the ratio between the $16m$ shear estimated from the ADCP measurements after filtering the sub-inertial frequencies and that of GM76.

Figure 13 displays the time-depth evolution of the eddy diffusivity. Strong variability is obtained with values within $[10^{-6}, 10^{-3}] m^2/s$. This range is consistent with typical values of 10^{-5} in calm regions (GM level) and up to 10^{-3} in the most turbulent regions. More precisely some spots of strong mixing can be related to the intense events just described (fig.6): the almost inertial storm generated IGW between days $15 - 25$, the 2 small spots around days 50 and 60 corresponding to internal tidal beams, winter-time events with the highest mixing values occurring around the most intense f spots at days 130, 140 and $170 - 180$ and eventually the $M2$ tidal beams at the end of the time series.

Finally a synthetic picture that summarizes the contribution of the near-inertial IGW to vertical

turbulent mixing is shown in Figure 14. A first comparison between depth-averaged quantities, namely the dimensionless kinetic energy level and the amplitude of the near-inertial frequency band, shows that most of the variability can be attributed to the near inertial IGW (Fig.14.b and c). Furthermore a good representation of the spatio-temporal distribution of the eddy diffusivity is obtained when the almost inertial component of the shear is retained only (Fig.14.a and d).

6. Conclusion

We focused our analysis on supra-inertial motions because of their importance in setting and controlling vertical mixing, as inferred from 13 month measurements at the North mooring, located at the middle of the northern boundary of the POMME area. A strong variability of the energy of these motions was obtained that could be mostly correlated either with atmospheric forcing or with larger scale motions.

We first isolated events of high amplitude IGW from the time evolution of the two prevailing frequency components, the inertial frequency and the semi-diurnal frequency. The horizontal kinetic energy in the inertial frequency band was typically higher than that of the $M2$ component by at least a factor of 4. The highest energy levels for the near inertial frequencies were observed between September and mid-April, with different mechanisms of generation that we attempted to isolate. By contrast internal tidal beams at the semi-diurnal frequency were found to be an almost permanent, though intermittent, feature all over the year. These beams could possibly be generated at a near-by seamount from which they would propagate through the mooring intermittently depending on stratification and larger scale velocity field.

First during fall, there was evidence of almost inertial waves propagating downward, down to at least $500m$. The energy flux associated with these waves and the time required for down-

ward propagation from the base of the mixed layer were estimated. It was thus possible to establish the link between the generation of these waves and the passage of storms. Evidence of storm generated IGW was previously provided by different authors (Leaman and Sanford, 1975, Pinkel, 1984), and most significantly during the dedicated field work "Ocean Storms Experiment" (D'Asaro, 1995.a). The estimated horizontal kinetic energy and vertical flux were of the same order as typical values during ocean storm experiment (Qi *et al*, 1995).

The most interesting observations with respect to the POMME experiment objectives occurred in winter, especially in January and February when the mixed layer deepening extended down to the depth of measurements. We thus got evidence of plume-like structure made of $\sigma = 27.1$ water induced by short-time period surface cooling events. The strong vertical motions associated with one plume very likely led to IGW generation in the underlying stratified waters. Both of these phenomena, upper-convection and IGW, led to intense mixing. Next, and during the shallowing of the mixed layer, spots of energetic waves appeared to be correlated with submesoscale structures, eddies or filaments. In particular for two of these events we gave evidence of IGW trapping within anticyclonic eddies. More generally the strong signature in temperature and salinity of these submesoscale features, indicate a southern origin. Thus they would result from instabilities occurring in this frontal region, possibly enhanced by the passage of storms. However, these structures could not be better identified than from the mooring measurements since their length scale is unresolved by the array measurements. Hence the intense winter-time events are either triggered by surface buoyancy loss or by submesoscale features. The first mechanism- IGW generation during winter-time convection- is an efficient mean for energy transfer into the wave field as shown by Garwood and Harcourt (1999) using LES at high latitudes. Our measurements suggest that this is as well the case at mid-latitude. However it appears that the frequency range of

the waves excited by convective plumes differ in these two cases: while an energy increase at the buoyancy frequency is observed in the former case, a strong signal near the inertial frequency, as well as at high frequency, is obtained here. It would be interesting to investigate whether these differences could be related to the spatial structure of the convective events.

Note that the winter-time events isolated here differ from the cooling events, mentioned by Large et al (1986) that were characterized by a SST decrease and an increase in temperature below the thermocline. These events were interpreted as the result of turbulent mixing induced by inertial motions favored by an inertial component of the wind (Large and Crawford, 1995). The late winter events observed in POMME are clearly of different nature. First there is no surface cooling but instead a net heat flux from the atmosphere to the ocean. Next, and more importantly, the TS variations are consistent with the advection of southern water across the front.

Due to the lack of T-S measurements the only possible estimate of eddy diffusivity was based on the vertical shear, with a stratification inferred from an inverse model (Gaillard *et al.*, this issue). A wide range of values, from $10^{-6}m^2/s$ up to $10^{-3}m^2/s$, was obtained, with a spatio-temporal distribution consistent with the intense events previously analyzed. Winter-time events led to the highest eddy diffusivity values and this enhances their importance regarding subduction and spring bloom.

This first characterization of IGW during POMME experiment showed the strong variability of these waves and the significant impact of intense events on energy fluxes and mixing. The most interesting point we shall further investigate is the analysis of the intense winter-time events isolated here. This includes intense surface cooling and interactions between IGW and larger

scale features. Indeed for the latter point, the analysis of winter-time events show wave trapping within sub-mesoscale eddies. It is hoped that the analysis of floats trajectories, next carried on, will provide further insights on these interactions as well as idealized direct numerical simulations focused on these events. Eventually the analysis of other moorings, located southward, should give a contrasting picture to that drawn here due to both weaker atmospheric forcing and mesoscale activity.

7. Acknowledgments

Notes

1. We checked that zooplancton motions do not bias significantly this signal

References

Assenbaum, M., Reverdin, G. 2004. Near-time analysis of the mesoscale circulation during the POMME experiment. *To appear in Deep Sea Res.*.

Caniaux, G., Brut, A., Bourras, D., Giordani, H., Paci, A., Prieur, L., Reverdin, G. 2004. A one year sea surface heat, fresh water and momentum budget in the North Eastern Atlantic basin during the POMME experiment: Part I: flux estimates. *to appear in J. Geophys. Res., special issue on POMME experiment*.

Caniaux, G., Belamari, G., Giordani, H., Paci, A., Prieur, L., Reverdin, G. 2004. A one year sea

surface heat, fresh water and momentum budget in the North Eastern Atlantic basin during the POMME experiment: Part II: flux correction. *to appear in J. Geophys. Res., special issue on POMME experiment.*

D'Asaro, E.A. 1985. The energy flux from the wind to near-inertial motions in the surface mixed layer. *J. Phys. Oceanogr.,* **15**, 1043-1059.

D'Asaro, E.A. 1995.a. A collection of papers on the Ocean Storms Experiment. *J. Phys. Oceanogr., 25,* 2817-2818.

D'Asaro, E.A., Eriksen, C., Levine, M., Niller, P., Paulson, C., van Meurs, P. 1995.b. Upper ocean inertial currents forced by a strong storm. Part I: Data and comparisons with linear theory. *J. Phys. Oceanogr., 25,* 2909-2936.

Gaillard F., Mercier, H., Kermabon, C. 2004. A Kalman filter for a synthesis of POMME physical data set. *to appear in J. Geophys. Res., special issue on POMME experiment.*

Garwood, R.W. Harcourt, R.R. 1999. Large-eddy simulation of pressure transport below the mixed layer. *Proc. 'Aha Huliko'a Hawaiin Winter workshop, January 1999, P. Muller and D. Henderson, Eds,* 189-196.

Giordani, H., Caniaux, G., Prieur, L. 2004.a. A simplified 3D oceanic model assimilating geostrophic currents: application to the POMME experiment. *Submitted to J. Phys. Oceanogr..*

Giordani, H., Caniaux, G., Prieur, L., Paci, A., Giraud, S. 2004.b. A one-year mesoscale simulation in the North-East Atlantic: mixed layer heat and detrainment-entrainment budget during the POMME experiment. *to appear in J. Geophys. Res., special issue on POMME experiment.*

Gregg, M.C. 1989. Scaling turbulent dissipation in the thermocline. *J. Geophys. Res., 94,* 9686-9698.

Klein, P., Llewellyn-Smith, S. 2001. Horizontal dispersion of near-inertial oscillations in a turbu-

lent mesoscale eddy field. *J. Mar. Res.,* *59*, 697-723.

Kunze, E., Sanford, T.B. 1984. Observations of near-inertial waves in a front. *J. Phys. Oceanogr.,*

14 566-581.

Kunze, E., Schmitt, R.W., Toole, J.M. 1995. The energy balance in a warm-core ring's near-

inertial critical layer. *J. Phys. Oceanogr.,* *25* 947-961.

Large, W.G., Mc Williams, J.C., Niiler, P.P. 1986. Upper-ocean thermal response to strong

autumnal forcing of the North-East Pacific. *J. Phys. Oceanogr.,* *16*, 1524-1550.

Large, W.G., Crawford, G.B. 1995. Observations and simulations of upper-ocean response to

wind events during the ocean storms experiment. *J. Phys. Oceanogr.,* *25*, 2831-2852.

Leaman, K.D., Sanford, T.B. 1975. Vertical energy propagation of inertial waves: A vector

spectral analysis of velocity profiles. *J. Geophys. Res.,* *80*, No.15, 1975-1978.

Lilly, J.M., Rhines, P.B. 2002. Coherent eddies in the Labrador sea observed from a mooring *J.*

Phys. Oceanogr., *32*, 585-598.

Osborn, T.R. 1980. Estimates of the local rate of vertical diffusion from dissipation measurements.

J. Phys. Oceanogr., *10*, 83-89.

Paci, A., Caniaux, G., Gavart, M., Giordani, H., Lévy, M., Prieur, L., Reverdin, G. 2004. A high

resolution simulation of the ocean during the POMME experiment. Part 1: Simulation results

and comparison with observations. *to appear in J. Geophys. Res., special issue on POMME*

experiment.

Paillet, J., Mercier, H. 1997. An inverse model of the eastern North Atlantic general circulation

and thermocline ventilation. *Deep Sea Res.,* *44A*, 1293-1328.

Pinkel, R. 1984. Doppler observations of internal waves: The wavenumber frequency spectrum.

J. Phys. Oceanogr., *14*, 1249-1270.

Figure 1.   Map of the Pomme region with the bathymetry displayed with a grayscale, the 5 moorings, North, South, East, West and Central, are indicated by the letters N, S, E, W and C. ADCP data, temperature and salinity measurements were only collected for two of them, N and S, data from the latter mooring were available later and therefore are not presented here. Note the Azores-Biscay ridge along the NE direction in between the Central and North moorings.

Polzin, K.L., Firing, E. 1997. Estimates of diapycnal mixing using LADCP and CTD data from 18S. *International WOCE Newsletter, 29*, 39-41.

Qi, H., De Szoeke, R.A., Paulson, C.A. 1995. The Structure of Near-Inertial Waves during Ocean Storms. *J. Phys. Oceanogr., 25*, 2853-2871.

Reverdin, G., Assenbaum, M., Prieur, L. 2004. The central waters during POMME (09/2000-09/2001) in the Northeast Atlantic. *to appear in J. Geophys. Res., special issue on POMME experiment.*

Tang, C.L.. 1979. Inertial waves in the Gulf of St. Lawrence: A study of geostrophic adjustment *Atmos.-Ocean, 17*, 135-156.

Valdivieso Da Costa, M., Mercier, H., Treguier, A.M. 2005. Effects of the mixed-layer time-variability on kinematic subduction rate diagnostics. *J. Phys. Oceanogr., in press.*

Van Haren, H. 2004. Bandwidth similarity at inertial and tidal frequencies in kinetic energy spectra from the Bay of Biscay. *Deep Sea Res., 51*, 637-652.

Woods, J.D., Barkmann, W. 1986. A lagrangian mixed layer model of the Atlantic 18C water formation. *Nature, 319(6054)*, 574-576.

8. Figure captions

Figure 2.   Time evolution of the atmospheric forcing at the North mooring starting on Sept. 22th, 2000 (data kindly provided by Caniaux *et al*, 2004.a and b):

a. Net heat flux (W/m^2); b. Wind stress (N/m^2); c. Wind direction (dg) respective to the West-East direction; d. Mixed layer depth inferred from a model using a Kalman filter (Gaillard *et al.*, this issue).

Figure 3.   Vertical temperature gradient computed from the 6 temperature time series, with $50m$ vertical separation, as a function of time and depth.

Figure 4.   Vector plot of sub-diurnal horizontal currents as a function of time and depth. A 2-day low-pass filter was applied to the ADCP time series. The maximum velocity is equal to $30 \, cm/s$.

Figure 5.   a. Horizontal kinetic energy (in $(cm/s)^2$) averaged over $[-480m, -240m]$ as a function of time of:

a. sub-diurnal currents, for comparison the maximum total kinetic energy is equal to $800 \, (cm/s)^2$ at $t \sim 170$ while the maximum 3 month average horizontal kinetic energy is much smaller equal to $150 \, (cm/s)^2$;

b. supra-inertial currents.

Figure 6.   a. Amplitude of the f component of the horizontal current from ADCP as a function of time and depth within $[240m, 480m]$;

b. Same as in a. but for the AAnderaa current meter, the arrows indicate the depth of the instruments;

c. Amplitude of the M2 component of the horizontal current from ADCP as a function of time and depth within $[240m, 480m]$;

d. Same as in c. but for the AAnderaa current meter, the arrows indicate the depth of the instruments.

For clarity only values greater than a threshold value of $20mm/s$ are represented. Note that the scales for f and $M2$ are the same.

Figure 7.   Near-inertial horizontal velocity as a function of time and depth during the first autumn storms:

a. eastward velocity component

b. northward velocity component.

Figure 8.   Correlation coefficient of the f component of the horizontal current within time interval $[10, 40]\,days$ with reference level at the upper depth $z = 240m$. The logarithm of this quantity is displayed for better visualization of the line of maximum correlation.

Figure 9.   a. Amplitude of the f component of the horizontal current;

b. Negative values of the vertical current averaged over two inertial periods;

c. Averaged vertical temperature gradient.

Figure 10.   a. Total surface heat flux (black line) and latent heat flux (gray line) at the North mooring (from Caniaux et al, 2004.a and b) during winter.

Temperature time series during winter at depth:

b. z=185m, the subsurface temperature ($z = 2m$) measured from a Carioca buoy that passed by the mooring around days $151 - 153$ is represented as well with a gray line; c. z=285m; d. z=385m.

Figure 11.   Evidence of an anticyclonic eddy passing by the North mooring around day 140 (following Lilly and Rhines, 2002):

a. Hodograph with time indicated by the color scale at depth $z = 400m$. b. Azimuthal velocity with isotherms superimposed; the vertical section is in the $E - NE$ direction with perpendicular velocity component represented with color scale; positive velocities are in the WNW direction. Evidence of an anticyclonic eddy passing by the North mooring around day 170:

c. Hodograph with time indicated by the color scale at depth $z = 300m$. d. Azimuthal velocity with isotherms superimposed; the vertical section in the $E - SE$ direction with perpendicular velocity component represented with color scale; positive velocities are in the NNE direction. Velocity and temperature have been averaged over two inertial periods for clarity.

Figure 12.   a. Amplitude of the M2 component of the horizontal current between mid-November and the end of December;

b. Filtered time series of the eastward and northward baroclinic velocity components.

Figure 13.   Eddy diffusivity inferred using Polzin's method (see text). Values are averaged over $6h$.

Figure 14.   a. Eddy diffusivity as in Fig.12;

b. Depth-averaged ratio between the horizontal kinetic energy and that of the GM spectrum;

c. Eddy diffusivity inferred from the vertical shear in the near-inertial frequency band only;

d. Depth-averaged amplitude of the f component of the horizontal current. Note that, as in

Figure 12, log_{10} of the eddy diffusivity is represented from -5 to -3 in a) and from -5 to -3.7
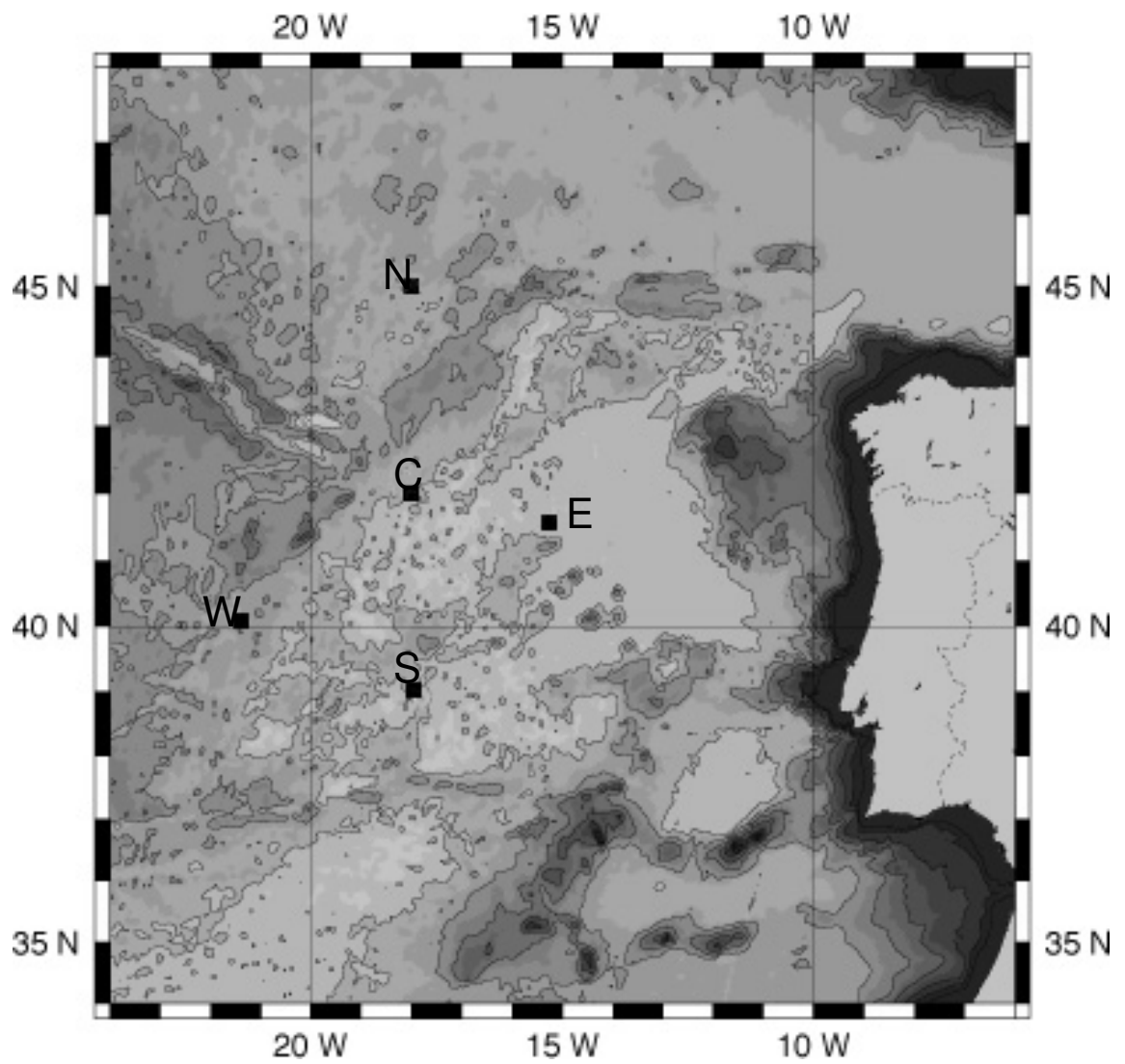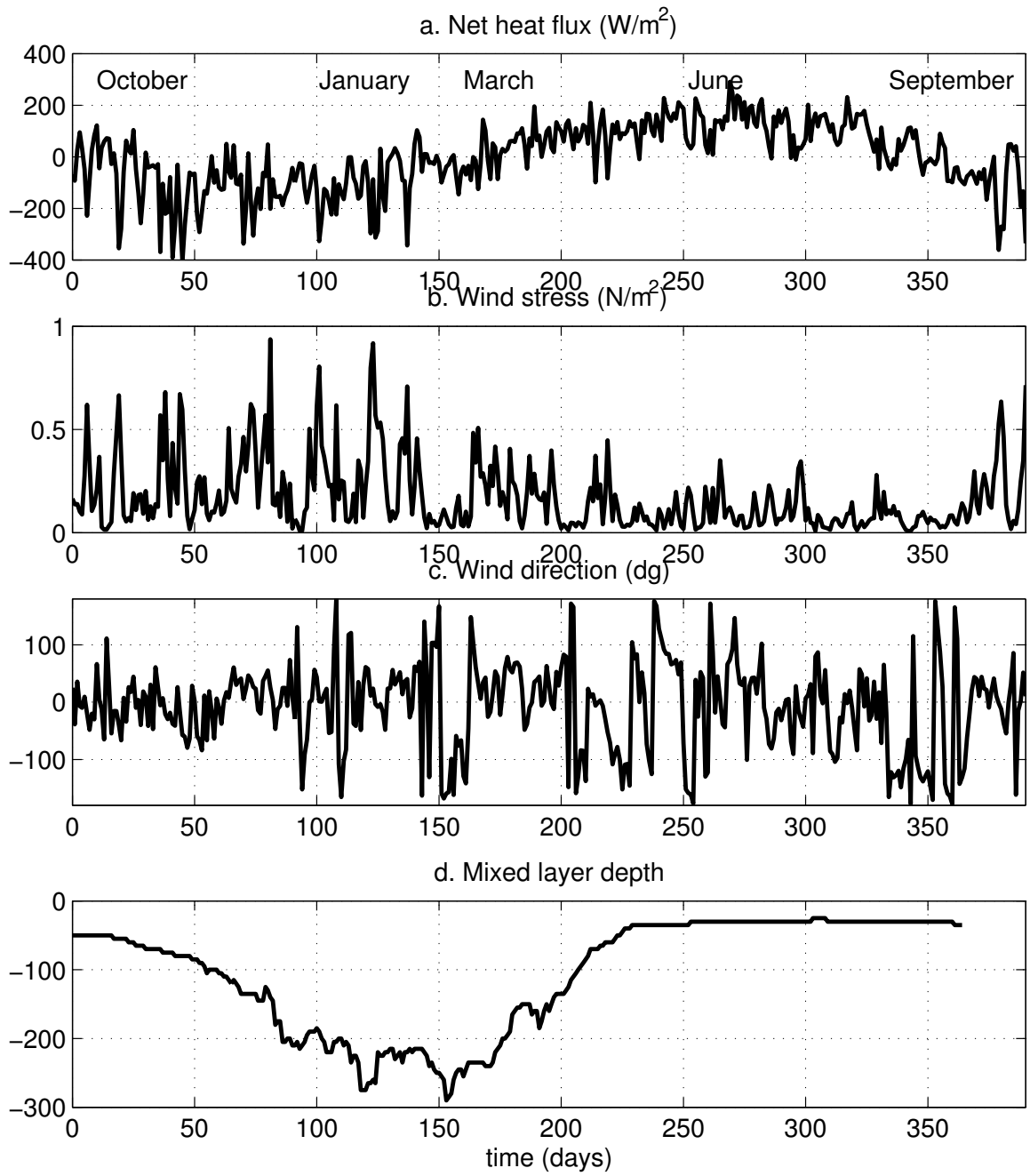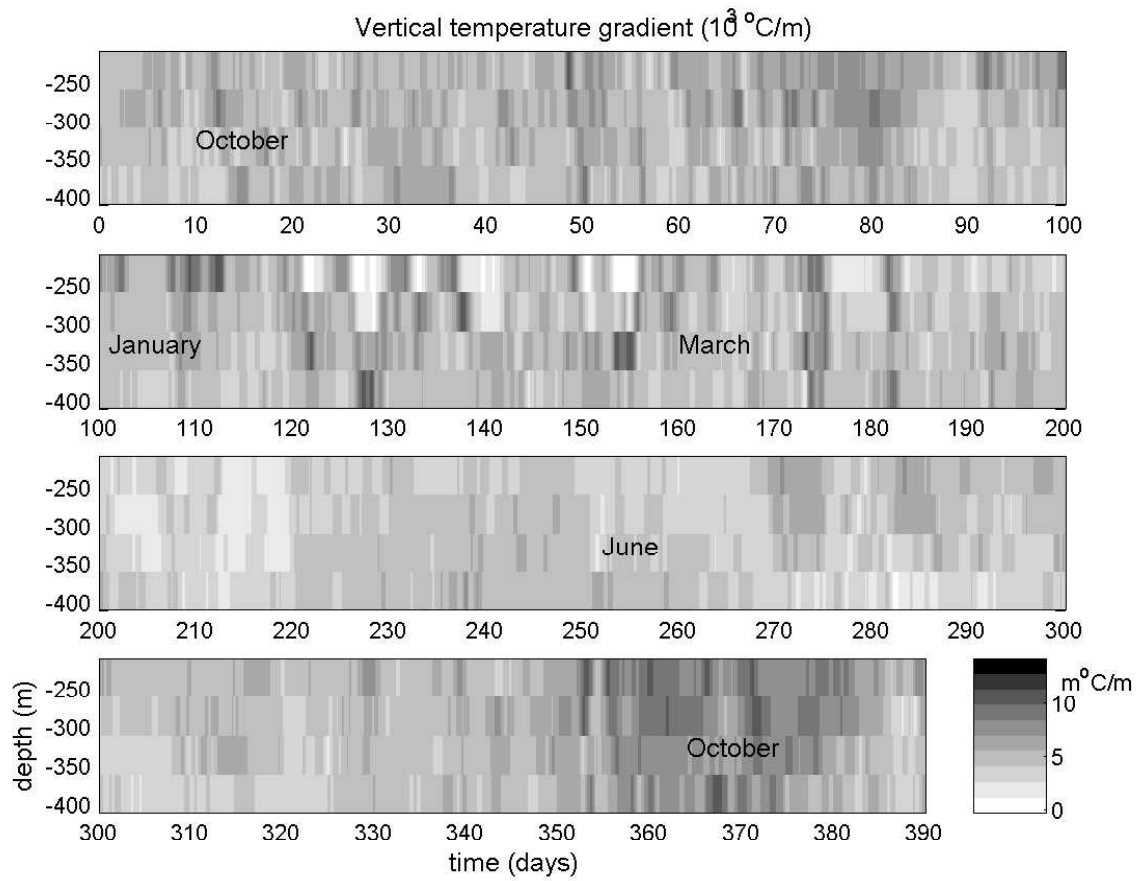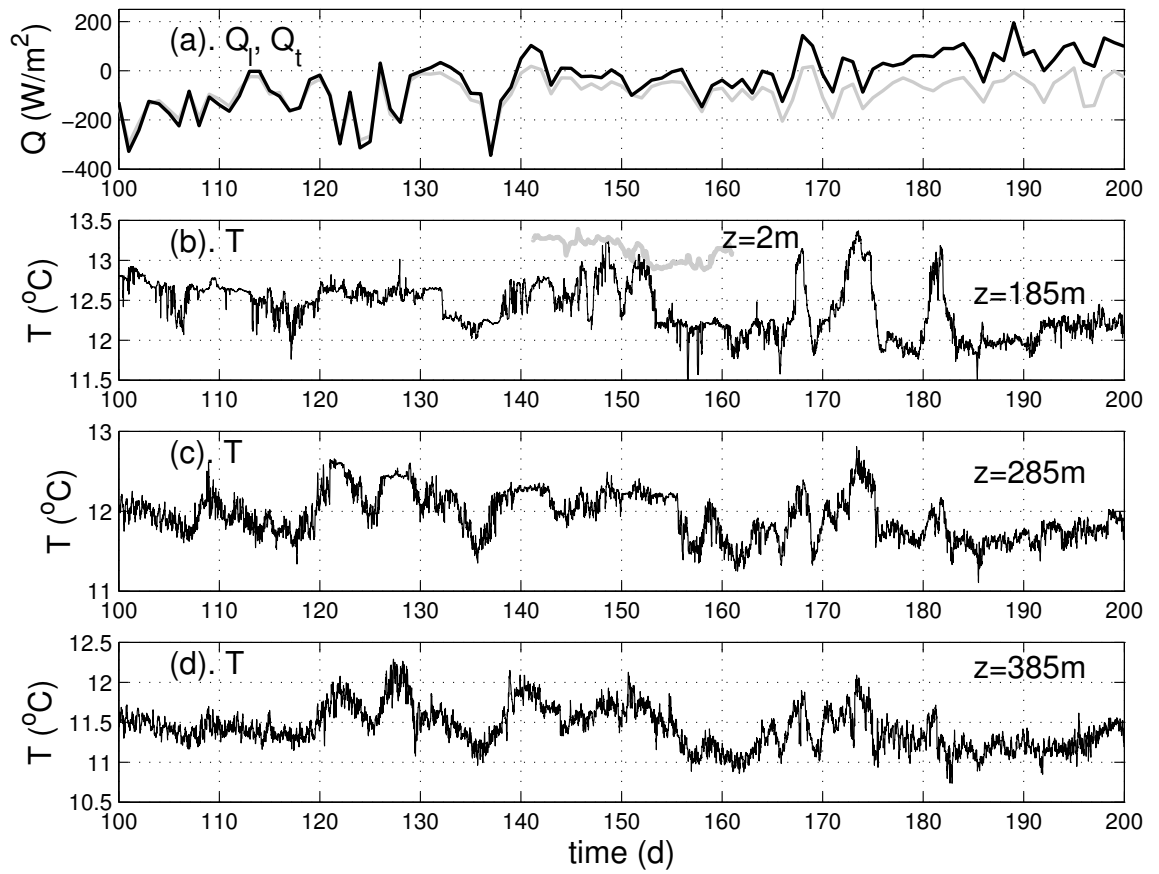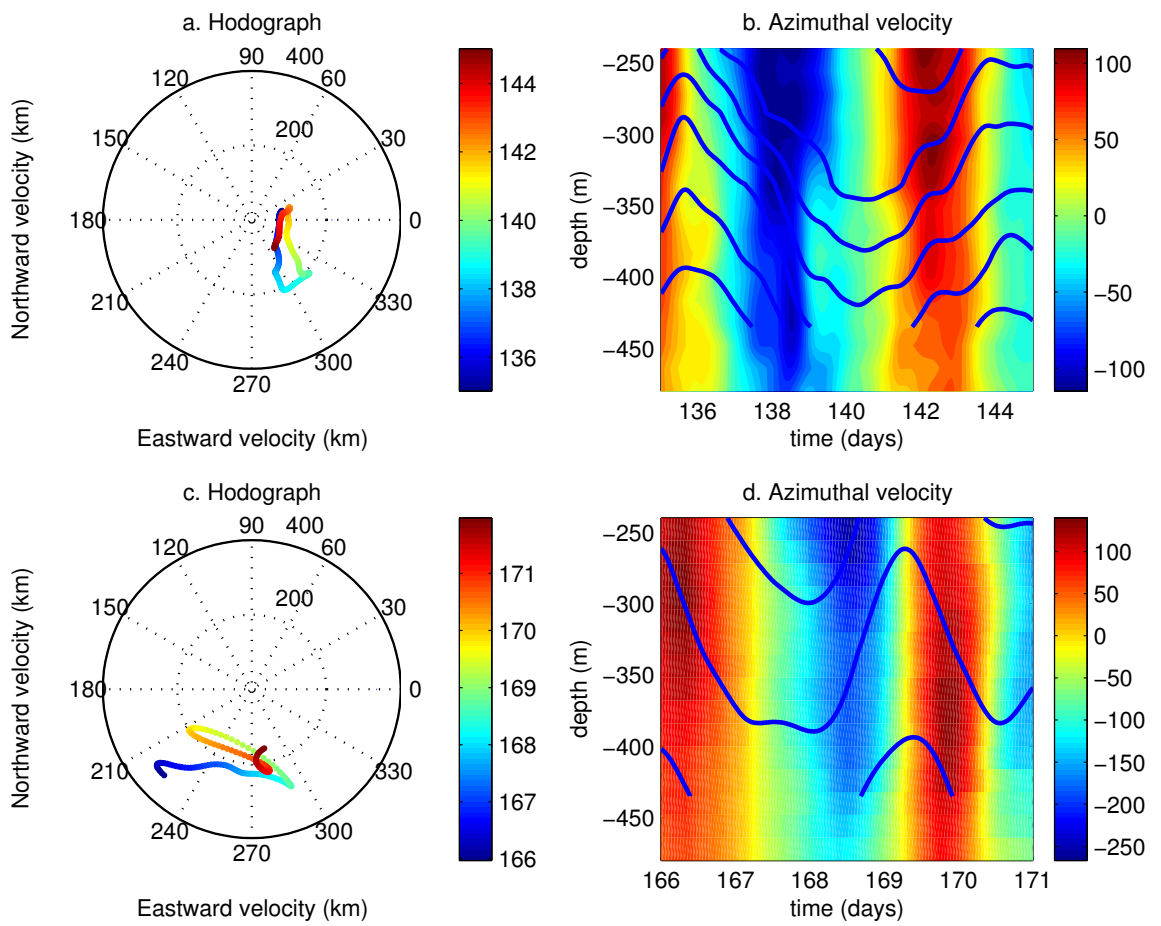
in c).

9 Figures

Figure 1:

Figure 2:

33

Figure 3:

Figure 4:

a. Horizontal kinetic energy of sub–diurnal motions

b. Horizontal kinetic energy of supra–inertial motions

Figure 5:

Figure 6:

a. Eastward velocity component

b. Northward velocity component

time (days)

Figure 7:

Modulus of the correlation coefficient (log$_{10}$)
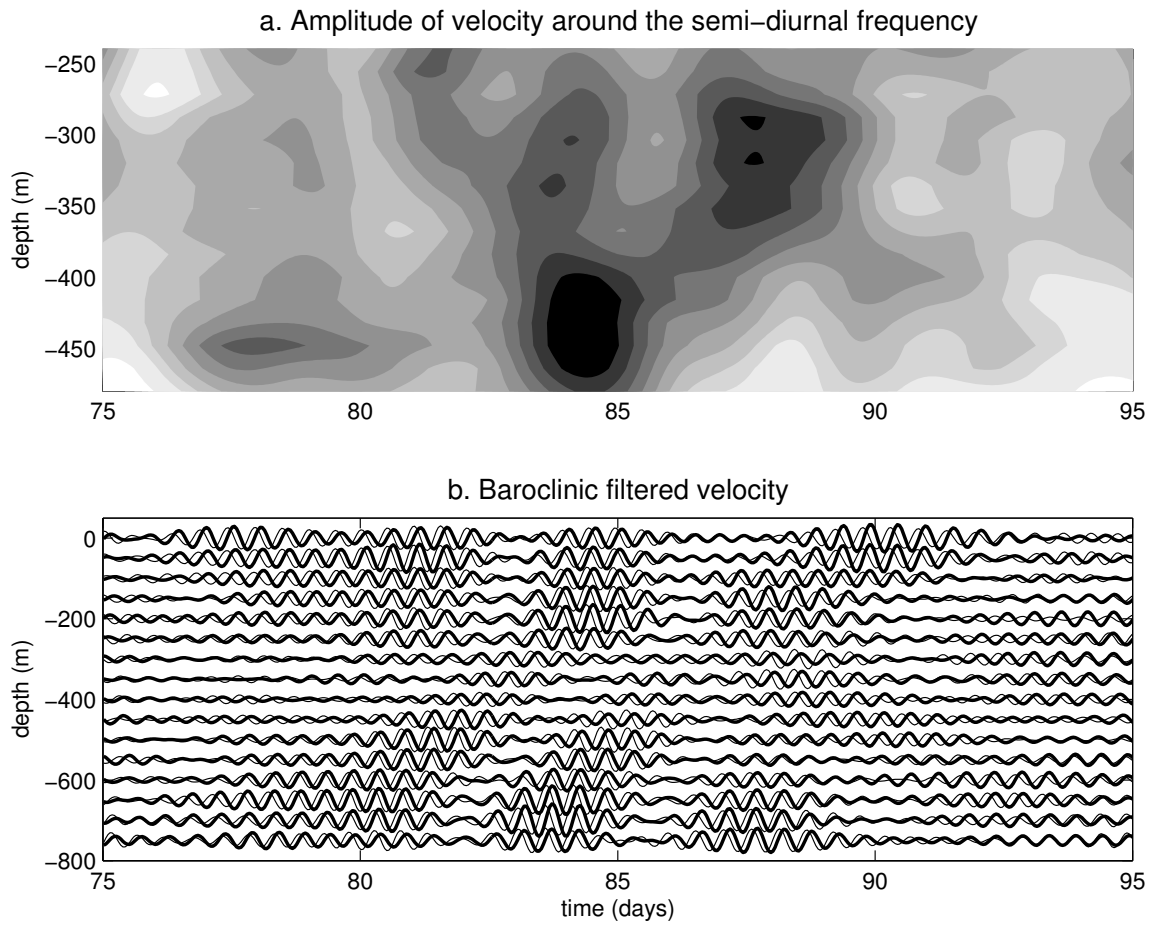

delay τ (d)
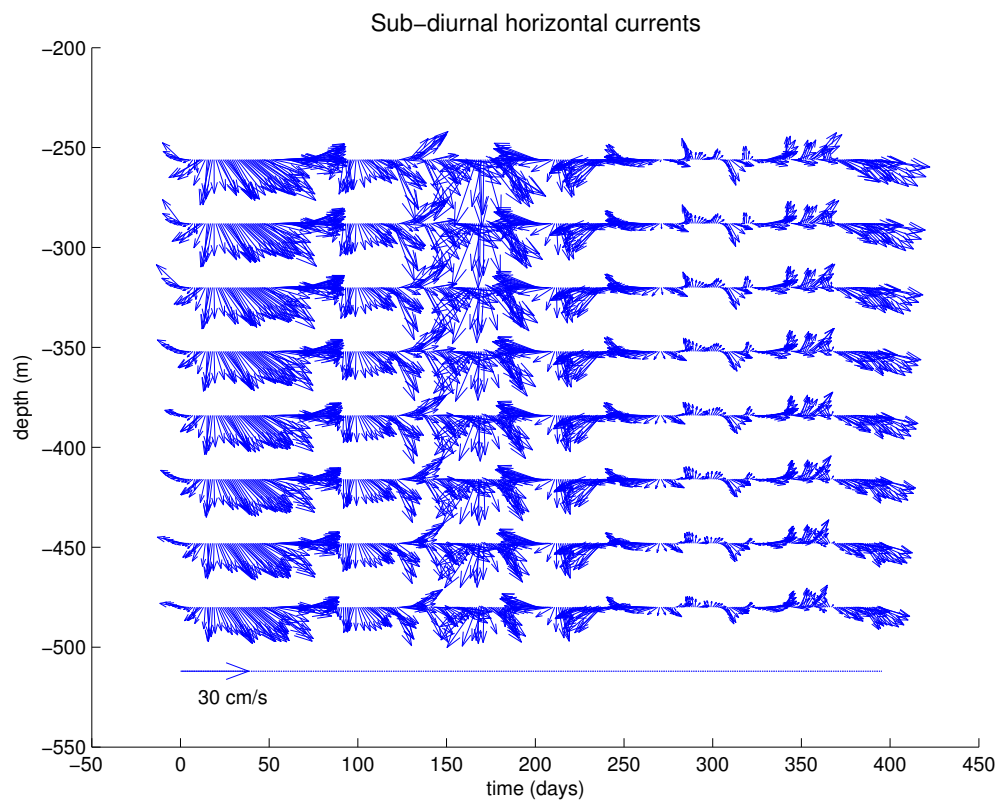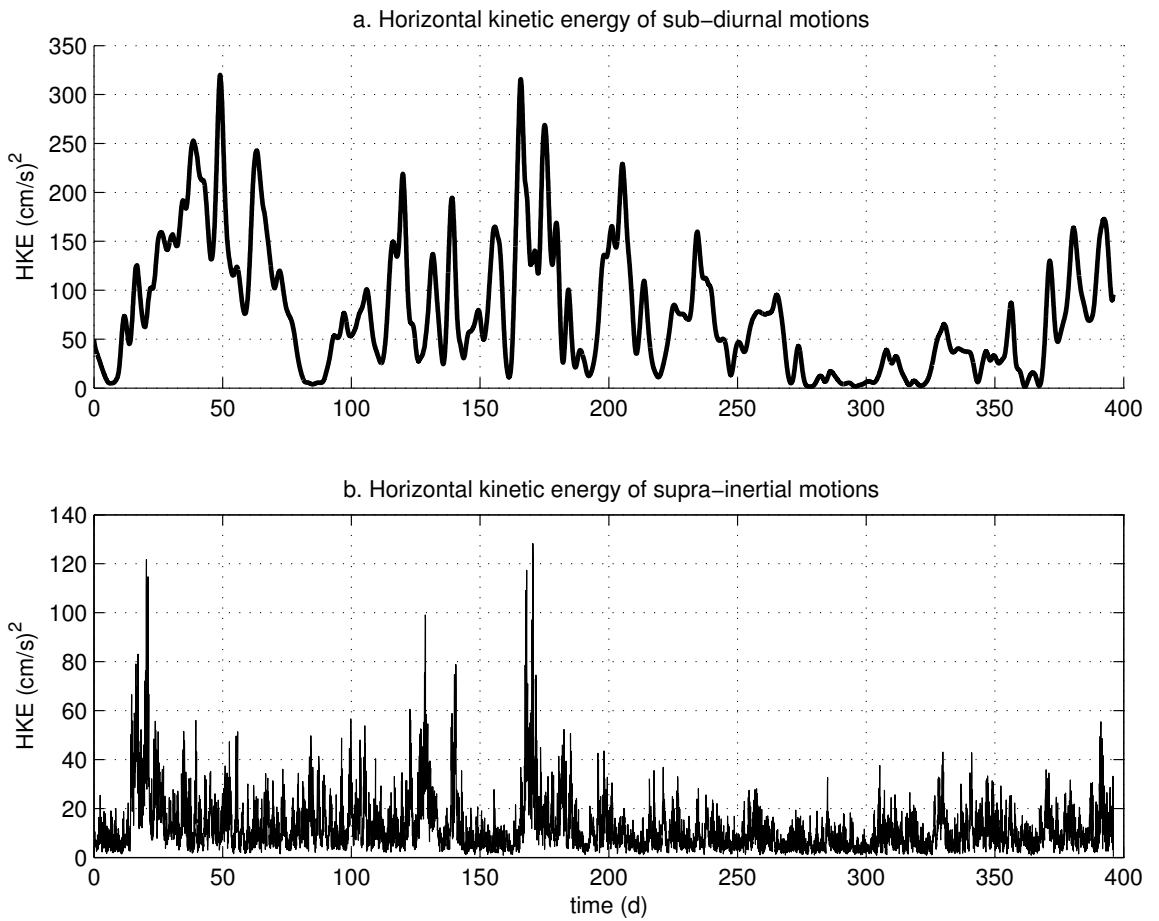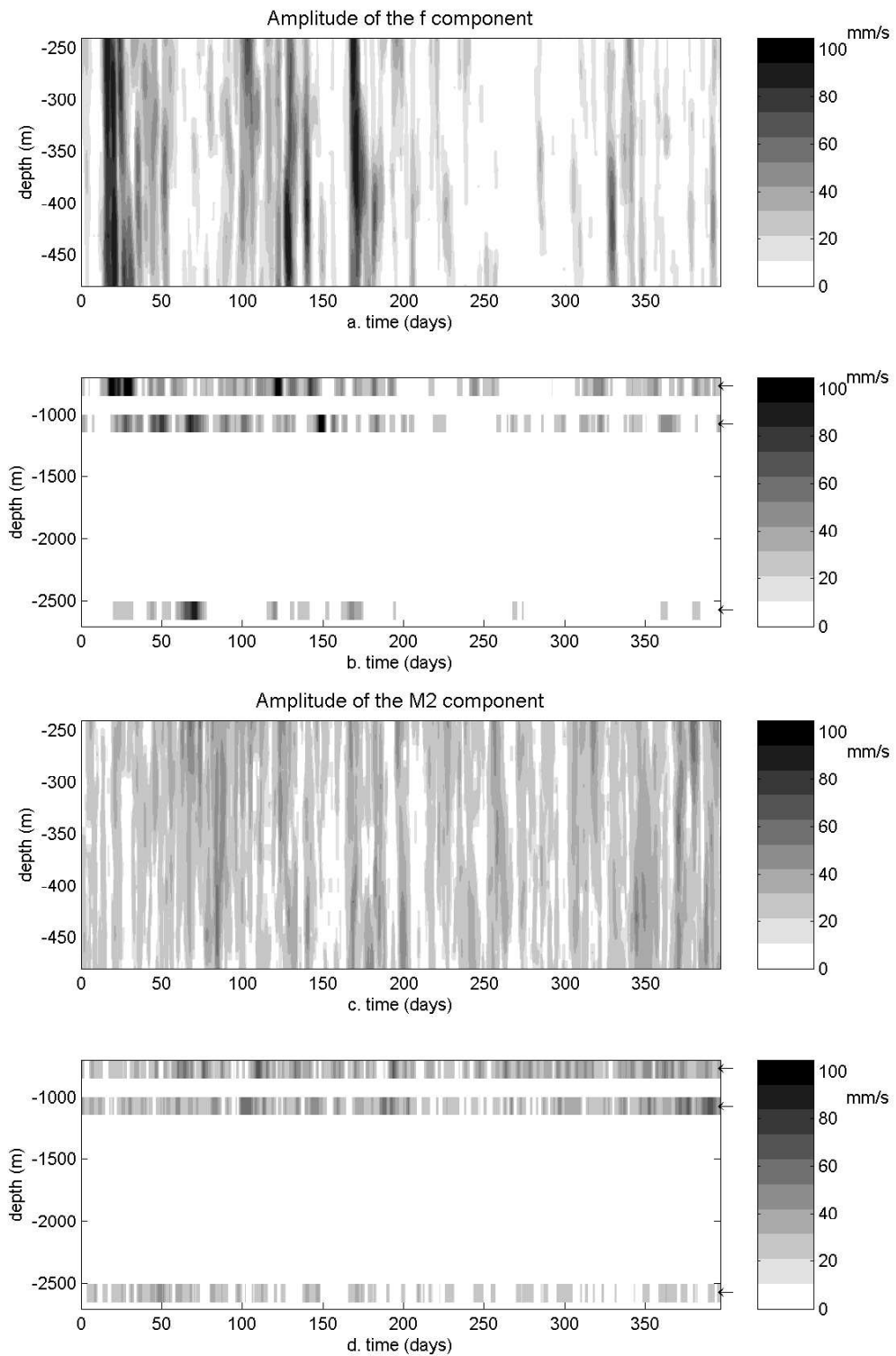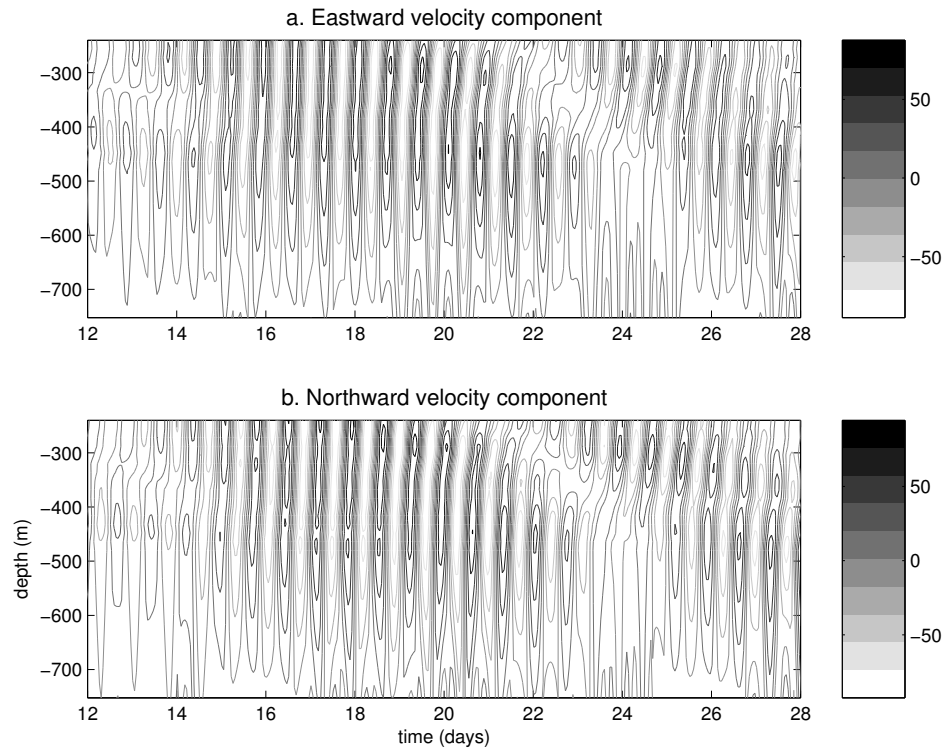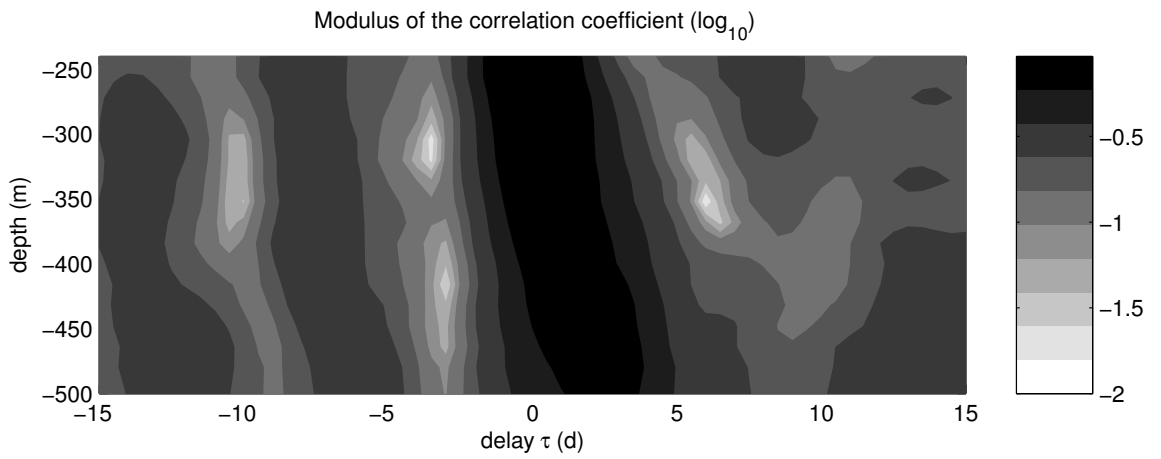
Figure 8:

38
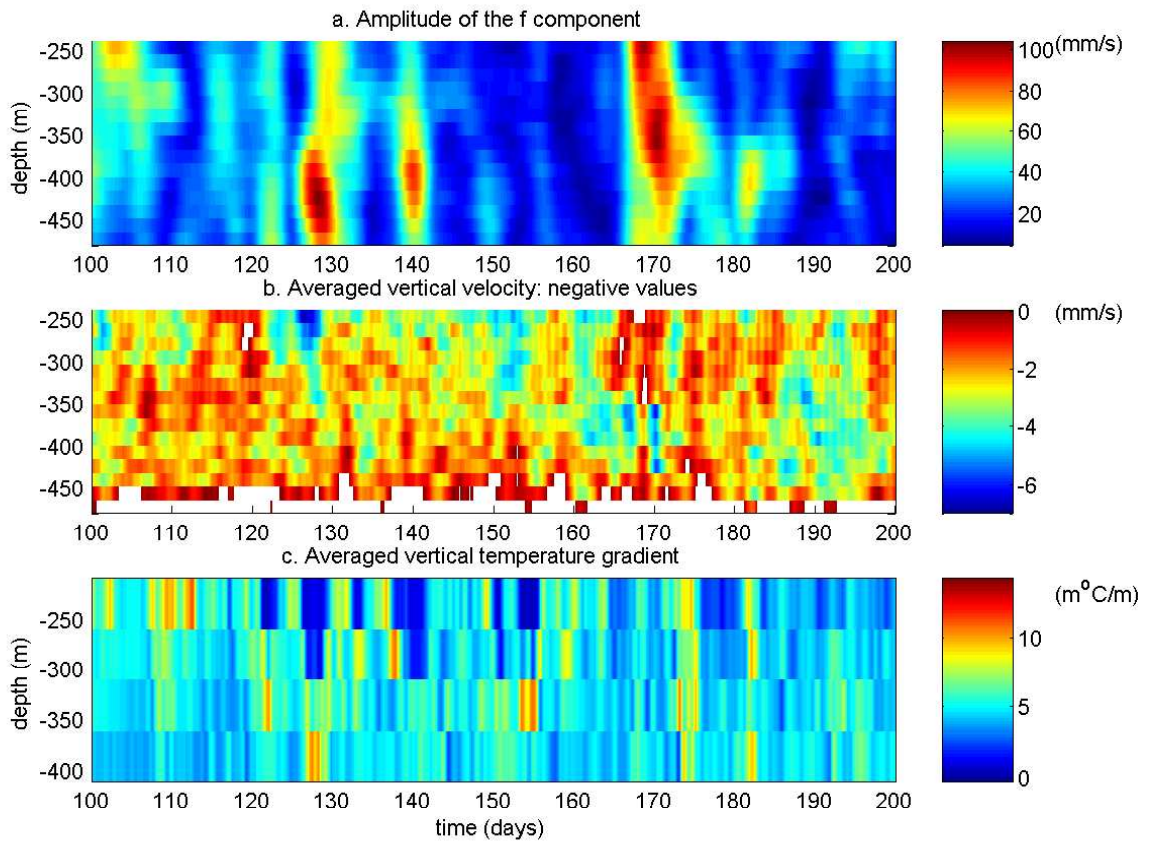
Figure 9:

Figure 10:

Figure 11:

a. Amplitude of velocity around the semi−diurnal frequency

b. Baroclinic filtered velocity

Figure 12:

Figure 13:

Figure 14: